Advances in Science and Technology
Research Journal

Advances in Science and Technology Research Journal, 2026, 20(4), 389–401
https://doi.org/10.12913/22998624/215387
ISSN 2299-8624, License CC-BY 4.0

Received: 2025.11.16
Accepted: 2026.02.15
Published: 2026.03.01

Ultrasonic beamforming for enhanced wind turbine inspection and safety

Michał Gołąbek[1], Barbara Stefaniak[1], Dariusz Wójcik[1,2], Tomasz Rymarczyk[1,2], Grzegorz Kłosowski[3], Monika Kulisz[3*]

[1] Research & Development Centre Netrix S.A., Związkowa 26, 20-704 Lublin, Poland
[2] WSEI University, Projektowa 4, 20-209 Lublin, Poland
[3] Lublin University of Technology, Nadbystrzycka 38D, 20-618 Lublin, Poland
* Corresponding author's e-mail: m.kulisz@pollub.pl

ABSTRACT

A portable cyber-physical phased-array ultrasonic system for in-situ wind-turbine blade inspection is presented. The prototype supports single scan acquisition and volumetric reconstructions via delay-and-sum beamforming with depth-dependent apodization, enabling real-time field operation on embedded hardware. The algorithmic pipeline combines dynamic receive aperture control, envelope detection, and lightweight post-filtering to provide metrologically reliable reconstructions suitable for automated re-porting and integration with digital workflows. Quantitative validation on 256 frames yields PSNR = 32.0–33.6 dB and SSIM = 0.867–0.908, confirming high reconstruction fidelity and stable acquisition required for robust volumetric sizing. Beyond imaging quality, a concise techno-economic model is used to quantify operations-and-maintenance impact under representative wholesale prices and capacity factors. Environmental and safety aspects align with these operational gains: compared with radiography, ultrasonic testing eliminates ionizing-radiation exposure, relative to penetrant or magnetic particle testing it reduces consumables and energy-efficient embedded processing with digital reporting keeps the device-level footprint secondary to the dominant benefits above.

Keywords: beamforming, non-destructive testing, image reconstruction, defect detection.

INTRODUCTION

Structural defects, such as cracks, porosity, delaminations, or foreign particle inclusions, pose a serious threat to the durability and safety of engineering components [1]. Their presence may lead to unpredictable failures and, consequently, to economic and ecological losses. Therefore, non-destructive testing (NDT) plays a key role in assessing the quality of materials and finished structures, as it enables defect detection without interfering with the structure of the tested object [2]. In operating wind farms, even moderate leading-edge erosion (LEE) of blades measurably depresses annual energy production (AEP) and drives derating and extra O&M interventions, so field-deployable diagnostics translate directly into avoided energy losses and service trips [3, 4].

A wide range of NDT techniques is currently applied, including ultrasonic testing (UT, PAUT, TOFD, guided waves) [5], radiographic testing (RT/DR/CR) [6], eddy current testing (ET/ECA) [7], magnetic particle testing (MT), liquid penetrant testing (PT), thermographic methods, and acoustic emission testing (AE) [8]. In addition to these methods, tomography-based imaging is widely used in practice, including X-ray computed tomography (XCT/μCT) [9], nuclear magnetic resonance or magnetic resonance imaging[10], ultrasound tomography (UST) [11, 12], electrical tomography [13, 14], and optical tomography [15–17]. Each of these techniques has specific advantages and limitations: radiography provides high-resolution imaging but requires radiation sources and specialized protection [18], penetrant and magnetic particle testing are relatively simple but generate chemical waste [19], thermography enables rapid inspection of large surfaces, but its accuracy depends on environmental conditions [20]. Recent reviews of condition monitoring and maintenance in the wind sector emphasize a shift to "digital" and non-contact methods (active thermography, shearography, microwaves) and to consistent data flows that reduce consumables and downtime [21, 22].

In recent years, modern ultrasonic systems have gained importance by integrating signal analysis, 2D/3D image reconstruction, and automated reporting of results [5, 23]. An example of such a solution is a portable phased-array ultrasonic platform equipped with a probe comprising 32–128 transducer elements capable of electronically steering ultrasonic beams to prescribed angles. This system enables non-invasive defect detection in a wide range of materials – from soft resins to steel alloys – while being energy-efficient by reducing power consumption in standby mode. Concurrently, phased-array UT based on full matrix capture (FMC) and total focusing method (TFM) has made fast, high-resolution 2D/3D reconstruction in composites more robust – including adaptive imaging, higher throughput, and better handling of curved surfaces – what directly supports volumetric assessment of bonded laminates in wind-turbine blades [24, 25] and complements recent demonstrations of accelerated inspections on composite blade panels [26]. These results are consistent with observations from impedance/capacitance tomography, where the integration of learning with reconstruction provides measurable benefits (time, resource consumption), strengthening the argument for sustainable, data-driven diagnostic procedures [27, 28].

Compared to classical NDT methods, the proposed phased-array ultrasonic system offers environmental benefits. Unlike radiographic testing, it avoids ionizing radiation, and unlike penetrant testing (PT) or magnetic particle testing (MT), it does not require chemicals or auxiliary agents [19, 29]. Digital signal processing and automated reporting reduce the consumption of consumables and paper and help limit retesting [2]. The combination of energy efficiency, waste-free operation, and broad diagnostic coverage aligns with sustainable development principles and yields a lower environmental footprint than many traditional quality-control methods.

The aim of this study is to present the measurement methodology of DefectoVision 3D and to discuss its potential contribution to sustainable non-destructive testing practices. DefectoVision 3D is a portable phased-array ultrasonic system developed and manufactured by Netrix S.A. (Lublin, Poland). The device has been designed as a commercial product and is dedicated for industrial deployment.

MATERIALS AND METHODS

To evaluate the applicability of DefectoVision 3D in practical NDT scenarios, a series of measurements was carried out using its integrated hardware and software modules. The device consists of an ultrasonic head, a power supply unit, and a portable case with a built-in touchscreen that serves as the user interface. Depending on the diagnostic requirements, data can be acquired and processed in one-dimensional (1D), two-dimensional (2D), or three-dimensional (3D) modes.

In the 1D mode, signals from selected transducers (1–128, depending on the head configuration) are recorded and displayed as amplitude versus time plots. This allows the analysis of wave propagation, including time-of-flight and reflections from material boundaries.

The 2D mode reconstructs cross-sectional images of the tested material using data from all active transducers. The resulting amplitude maps can be adjusted by modifying the gain parameter, enabling improved visualization of discontinuities within the sample.

In the 3D mode, data are acquired incrementally as the head is moved across the material surface. Position tracking is provided by a measurement trolley equipped with an encoder, accelerometer, and gyroscope, which ensures accurate determination of the spacing between measurement frames. During acquisition, a simplified real-time visualization is available, while the final reconstruction is generated in the form of a point cloud, enabling spatial analysis of defect distribution.

Hardware

DefectoVision 3D is designed as a small case with a 9-inch IPS touch screen on the front panel. The device is fully portable as it has a built-in li-ion battery pack that allows for uninterrupted operation for up to approximately 6 hours. On the sides of the screen there are located LED strips to indicate the operating status of the device. Behind the screen, on the back side of the device's housing, there is a power switch and a charger connector, a USB port, an ETHERNET port, and a socket for connecting an ultrasonic probe.

DefectoVision 3D (Figure 1) is an integrated measurement system consisting of:

- Raspberry Pi 5 minicomputer, which analyzes tomographic data from the measuring hardware and displays it in the form of a reconstruction on the screen on the built-in graphical interface
- Motherboard, connecting all device modules into one compact measurement system. The board has an STM32F7 microcontroller installed, which is used to control the charging process, parameterize FPGA circuits, control LED strips, control cooling fans, store parameters in FRAM memory, communicate with the sliding carriage (CAN or WiFi) and control the switching of ultrasonic multiplexers. The motherboard also features an Intel Cyclone IV FPGA chip, which is responsible for controlling and receiving data from 4 measurement cards and transferring it via USB3.0 to Raspberry Pi.
- 8-channel measurement cards – are made using Intel FPGA Cyclone V and integrated Analog Devices MAX2082 analog front end (AFE) chips. Each channel of the measurement card has its own high-voltage pulse generator, T/R switch, LNA (low noise amplifier), VGA (variable gain amplifier) and 25MSPS ADC converter with LVDS serialization.
- 1:4 MUX – switches 32 active measurement channels between 4 sectors of the measurement matrix transducer, allowing the device to work with transducers having 128 measurement crystals.
- BMS and battery back – a module protecting the 4S pack against overcharging, excessive discharge and with passive balancing

Figure 1. DefectoVision 3D

The DefectoVision 3D has a built-in wireless communication module that is used to exchange data with the sliding carriage. The sliding carriage is designed to accurately monitor the position of the ultrasonic head during 3D scanning (Figure 2).

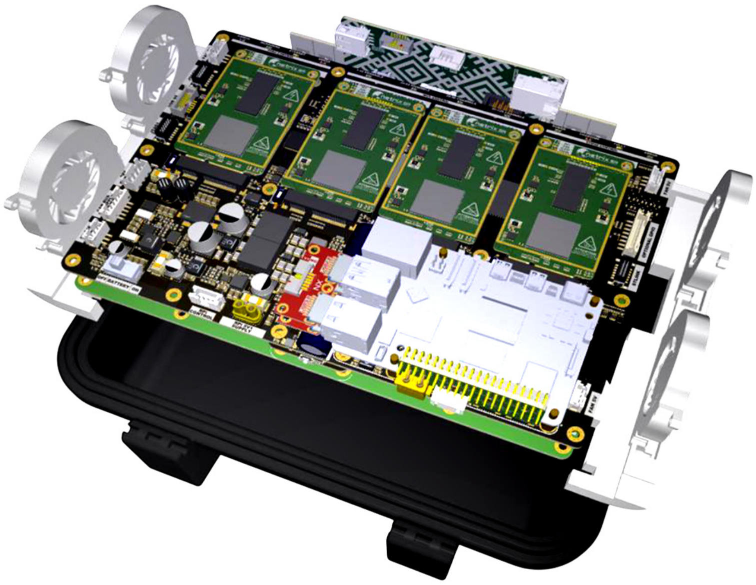

Figure 2. 3D model of DefectoVision 3D hardware construction

The trolley's axles are designed to adapt to uneven surfaces (cushioned suspension). Inside the trolley there is a small lithium-ion battery, a charging system, and an RGB LED indicating the status of the device. The USB-C charger port is hidden in the lower part of the housing. The overall structure of the developed ultrasound imaging system is presented in Figures 3 and 4, which illustrate the software and hardware architecture, respectively.

Software system architecture overview

The presented DefectoVision 3D system implements a multi-tier software architecture specifically designed to achieve optimal computational efficiency, minimal power consumption, and real-time performance in ultrasonic nondestructive testing applications. The architecture follows a distributed computing paradigm with three primary computational layers: a high-performance backend reconstruction engine, an interactive web-based frontend interface, and a centralized update management system. This design philosophy ensures maximum utilization of available computational resources while maintaining system responsiveness and energy efficiency.

The backend subsystem, implemented in Python with PyTorch acceleration, serves as the computational core for advanced beamforming algorithms and signal processing operations. The system architecture incorporates Redis-based inter-process communication queues that enable asynchronous data flow between measurement acquisition, reconstruction processing, and visualization components. This queue-based approach significantly reduces CPU blocking operations

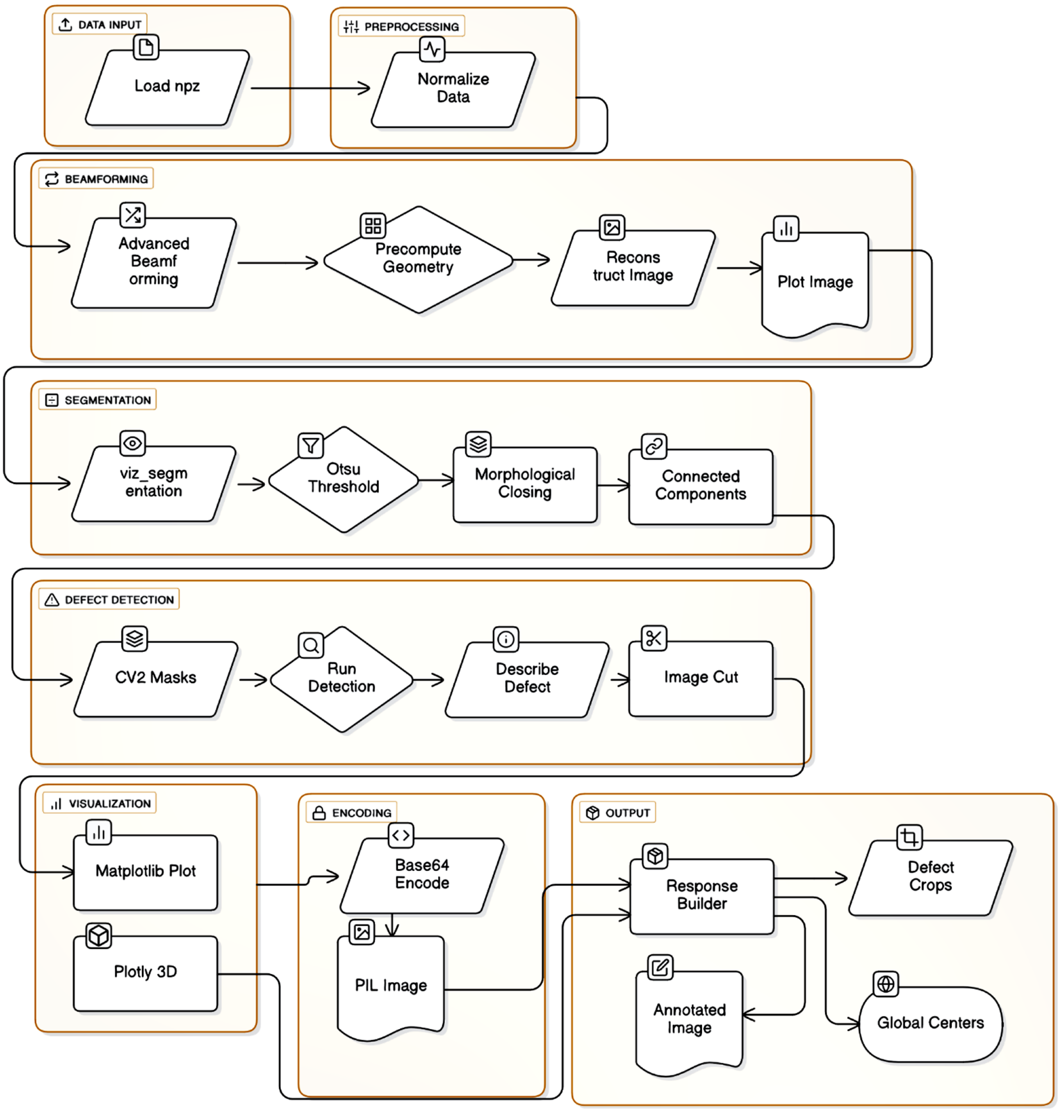

Figure 3. Software architecture and data processing pipeline implemented in DefectoVision3D

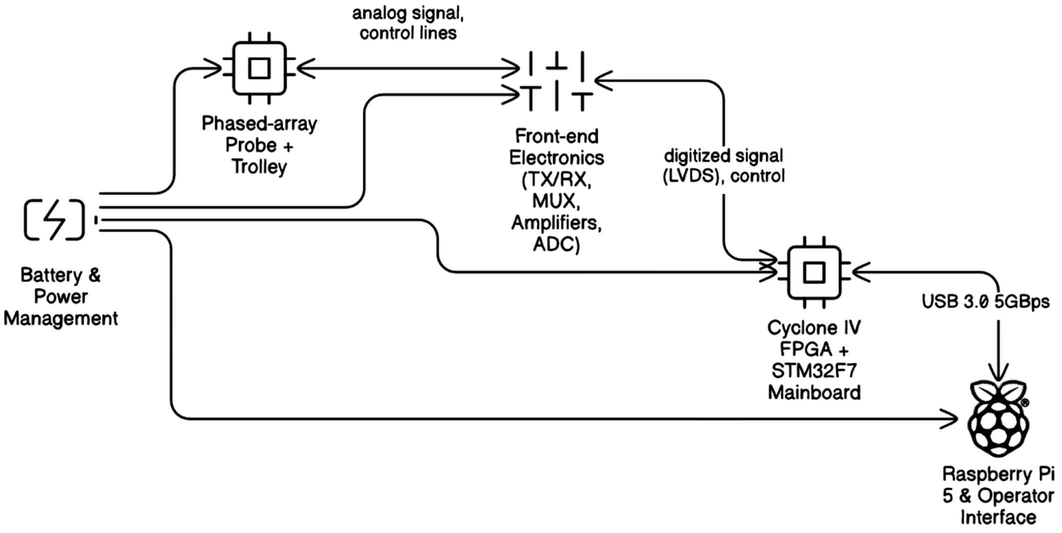

Figure 4. Schematic diagram of the hardware architecture of the developed DefectoVision3D

and enables optimal load distribution across available processing cores, resulting in substantial improvements in overall system throughput and power efficiency.

The system implements a sophisticated Redis-based data queue management system that optimizes CPU utilization through intelligent load balancing and backpressure handling. The RedisDataQueueManager [30] coordinates data flow between measurement acquisition, reconstruction processing, and frontend visualization components using separate queues for measurement data and reconstruction results. This architecture enables pipeline parallelism with configurable queue sizes to balance memory utilization and processing latency [31].

The queue management system incorporates performance monitoring capabilities that track queue utilization, processing throughput, and system resource consumption. Automatic backpressure mechanisms prevent queue overflow conditions and maintain system stability during high-throughput inspection operations. The implementation utilizes pickle serialization for efficient data transfer while maintaining data integrity across process boundaries.

The asynchronous processing architecture enables the system to maintain consistent frame rates even during computationally intensive reconstruction operations. By decoupling data acquisition from processing and visualization, the system achieves optimal resource utilization and minimizes power consumption through intelligent workload scheduling.

The frontend subsystem implements a modern React-based web application with real-time WebSocket communication for live data visualization and system control. The interface utilizes the Next.js framework with TypeScript for type-safe development and optimal performance characteristics. The system supports multiple visualization modes including 2D B-scan displays, 3D volumetric reconstruction, and real-time signal analysis with interactive parameter adjustment capabilities.

Advanced visualization components utilize hardware-accelerated rendering through WebGL and Three.js libraries to achieve smooth real-time display performance on device. The interface implements intelligent caching mechanisms and progressive loading strategies to minimize memory consumption while maintaining responsive user interactions. Battery usage optimization is achieved through adaptive frame rate control and selective rendering based on user activity patterns.

The overall system architecture achieves significant performance improvements through several optimization strategies specifically designed for embedded ARM computing platforms. The Redis queue system eliminates processing bottlenecks and enables sustained throughput of up to 40 frames per second during continuous inspection operations on Raspberry Pi 5 hardware. Memory optimization techniques, including tensor memory pooling and garbage collection management, maintain stable operation during extended inspection sessions [32].

Power consumption optimization is achieved through dynamic clock scaling, adaptive processing load management, and intelligent component sleep scheduling. The system automatically reduces computational intensity during idle periods and implements progressive shutdown of unused subsystems. Additionally, the hardware incorporates an intelligent auto-shutdown mechanism that activates after 15 minutes of inactivity, ensuring minimal power consumption during standby periods. These optimizations result in overall reduced power consumption compared to conventional ultrasonic inspection systems while maintaining equivalent or superior inspection capabilities.

The modular architecture enables future expansion and integration of advanced signal processing techniques, machine learning-based defect classification algorithms, and enhanced visualization capabilities. The system's design ensures scalability for deployment in various industrial inspection environments while maintaining consistent performance characteristics and energy efficiency standards.

Algorithms

The reconstruction of ultrasonic data in DefectoVision 3D is performed using the delay-and-sum (DAS) beamforming algorithm with envelope detection, which is a standard yet robust method for generating 2D and 3D images from multi-element transducer arrays. In this approach, the signals acquired by individual transducers are first time-shifted to compensate for differences in propagation paths between the emitter, reflector, and receiver. This time alignment ensures that echoes originating from the same spatial location add constructively, thereby enhancing the signal-to-noise ratio (SNR) of true reflectors while suppressing incoherent noise and artifacts [33].

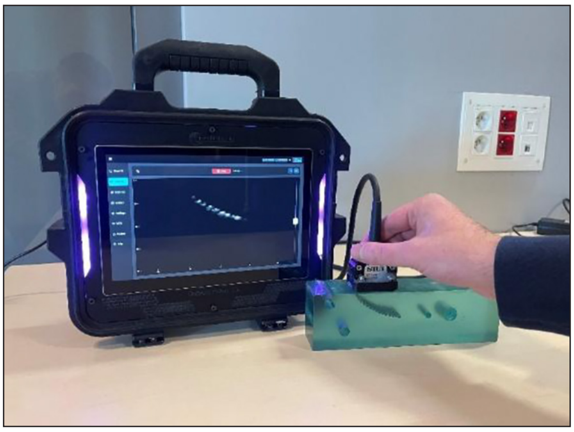

Figure 5. Tested object

Mathematically, the reconstructed image intensity at a spatial point (x, y) is defined as:

$$I(x,y) = \sum w_t(x,y) \cdot s_t(\tau_t(x,y)) \cdot \alpha(x,y) \quad (1)$$

where: $w_t(x, y)$ are apodization weights applied to reduce sidelobes and improve lateral resolution, s_t represents the signal received at transducer element t, τ_t denotes the propagation delay corresponding to the distance between the transducer and the imaging point (x, y), $\alpha(x, y)$ is an amplitude compensation factor that corrects for attenuation losses and geometrical spreading.

Once the beamformer signal is obtained, envelope detection is applied, typically via the Hilbert transform, to extract the magnitude of the analytic signal. This step removes oscillatory components of the raw RF signal, yielding a smooth intensity distribution that is directly interpretable as an image. This method provides a good compromise between computational simplicity and imaging quality. Although more advanced techniques such as adaptive beamforming or model-based inversion exist, the delay-and-sum algorithm remains attractive for real-time and portable systems such as DefectoVision 3D, where energy efficiency and robustness are important considerations.

RESULTS

The performance of the DefectoVision 3D (Figure 5) system was evaluated through a multi-level analysis encompassing single-signal acquisition, two-dimensional (2D) reconstruction, and three-dimensional (3D) point cloud visualization. The 1D and 2D experiments were carried out on a calibration block manufactured from polyepoxide (epoxy resin), which contained a row of eight through-thickness cylindrical holes acting as artificial defects. The block thickness was 38 mm and the nominal diameter of each hole was 2.4 mm.

The analysis of individual A-scans confirmed high-quality data acquisition. Primary echoes and reflections originating from internal defects were unambiguously identifiable. As illustrated in Figure 6, the initial signal peak (observed around the 50th recorded point) corresponds to the system excitation, while the subsequent prominent maximum (visible near the 400th point) is attributed to the reflection from a defect. The high signal-to-noise ratio facilitated reliable detection of

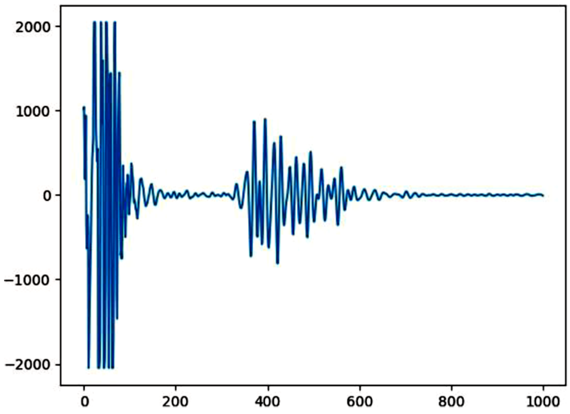

Figure 6. Exemplary A-scan signal acquired from a defective sample. The first major peak represents the excitation signal, while the second indicates a reflection from an internal defect

relevant ultrasonic features. The selection of the transducer type was found to significantly influence the sensitivity for defect detection, particularly in the context of smaller discontinuities. These findings confirm that the system provides a robust and high-fidelity data foundation necessary for subsequent 2D and 3D imaging.

Two-dimensional reconstructions were generated by applying the delay-and-sum beamforming algorithm followed by envelope detection. The resulting amplitude maps effectively revealed the spatial distribution of defects within the inspected samples. The adjustment of key imaging parameters, such as gain and apodization functions, was found to have a measurable impact on image clarity and defect visibility. The application of optimized parameter settings enabled accurate visualization of defect morphology, including their shape and orientation.

Figure 7 presents the reconstruction pipeline: testing object, the initial B-scan image, the result of segmentation using multiscale Otsu thresholding [34, 35] to isolate defects, and the final image with computed centroids for distinguishable objects. This processing sequence allows for the automated generation of inspection reports, which include quantitative measurements of defect dimensions such as width, height, and cross-sectional area.

To quantify the geometric accuracy of the 2D reconstructions, the automatically detected defect centroids were compared with reference positions defined from the calibration block geometry. The analysis was performed for eight artificial reflectors. The mean absolute localisation error (MAE) in the vertical direction was 0.88 mm, while in the horizontal direction it was 0.53 mm, yielding an overall MAE of 0.70 mm. The root-mean-square localisation error, computed from the mean squared error (MSE) across all analysed defects was 2.99 mm. These values demonstrate millimetre-level positioning accuracy, which is sufficient for typical acceptance criteria in wind-turbine blade inspection and confirms that the reconstructed defect dimensions are metrologically meaningful rather than purely qualitative.

Three-dimensional analysis was performed by acquiring a sequence of parallel 2D B-scans during a controlled, linear translation of the ultrasonic probe. Spatial consistency between consecutive frames was maintained using data from an integrated motion-tracking unit. This ensured precise registration of each scan position, enabling accurate volumetric reconstruction.

The resulting three-dimensional point clouds enable comprehensive volumetric visualization of internal defects, supporting the assessment of their spatial extent, orientation, and interconnections. The system provides two primary visualization modes: a raw point cloud representation and orthogonal cross-sectional planes. Figure 9 shows the point cloud reconstruction of the test phantom presented in Figure 8, which contains the inscribed

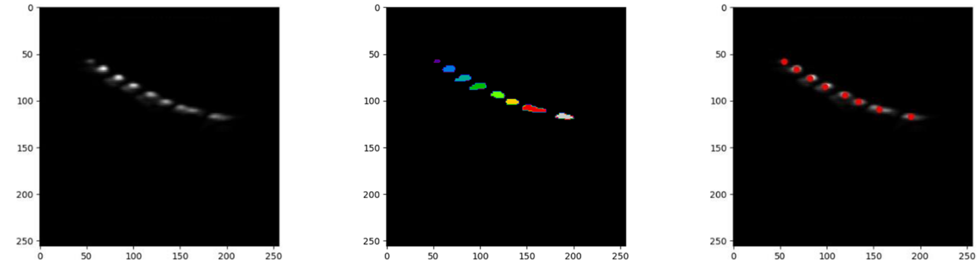

(a) Raw reconstruction (b) Segmented defects (c) Detected centroids

Figure 7. Two-dimensional reconstruction results: (top) tested object; (bottom row) (a) raw, (b) segmented, (c) centroids

Figure 8. Photograph of the resin calibration phantom featuring the inscribed word "NETRIX" used for system validation

letters "NETRIX". The experiment involved moving the probe-mounted cart along the smooth surface of the phantom (without the inscription, which during the test was oriented downward). Figure 10 presents the corresponding orthogonal cross-section (YZ-plane) through the reconstructed volume, further revealing the internal structure.

A quantitative evaluation against reference models confirmed the high fidelity of the reconstructed images. The analysis was performed on a dataset of 256 frames, collected using an ultrasonic probe mounted on a dedicated, automated scanning carriage. The trajectory registration system continuously tracked the probe's position and precisely measured the distance traveled from the starting point, ensuring high spatial accuracy for each successive scan.

The application of objective image quality metrics provided tangible data confirming the system's effectiveness. Peak signal-to-noise ratio (PSNR) values, ranging from 32.0 dB to 33.6 dB, indicate very high signal reconstruction fidelity and a low level of distortion. Meanwhile, structural similarity index (SSIM) values in the range of 0.867 to 0.908 demonstrate excellent preservation of image structure and accurate reproduction of the geometric features of the detected discontinuities. According to widely accepted criteria in the literature [36, 37], the obtained value ranges for both metrics classify the reconstruction quality as very good, with an acceptable, low level of distortion and high structural similarity to the reference model.

The statistical distribution of PSNR and SSIM values for each of the 256 analyzed frames is presented in Figure 11. The low variability of both metrics between successive frames (small standard deviations) confirms the stability of the acquisition system and the reproducibility of measurements during probe movement.

In summary, the combined results of the quantitative and qualitative assessments demonstrate that the DefectoVision 3D system reliably detects and visualizes internal defects. The combination of high-quality single signals (A-scan), clear 2D reconstructions, fully spatial 3D representations, and positive, objective image metrics confirms the system's capability to perform accurate and fully reproducible inspections across all levels of analysis.

DISCUSSION

The proposed portable 3D ultrasonic inspection platform addresses pressing needs in wind-turbine maintenance within a market projected to expand from $7.0 billion in 2024 to $11.5 billion by 2028 (10.5% CAGR). This growth, coupled with the scale of global deployment, underscores the demand for efficient, field-ready NDT solutions for blades and related components [38]. With global installed wind capacity reaching 1.174 GW in 2024 [39] and approximately 400,000 turbines worldwide requiring regular inspection [40], the

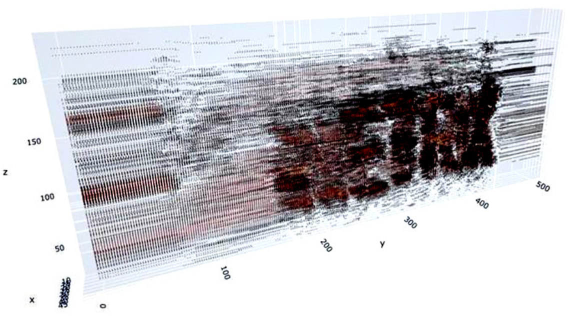

Figure 9. Three-dimensional point cloud reconstruction of the defects within the "NETRIX" phantom, visualizing the volumetric data

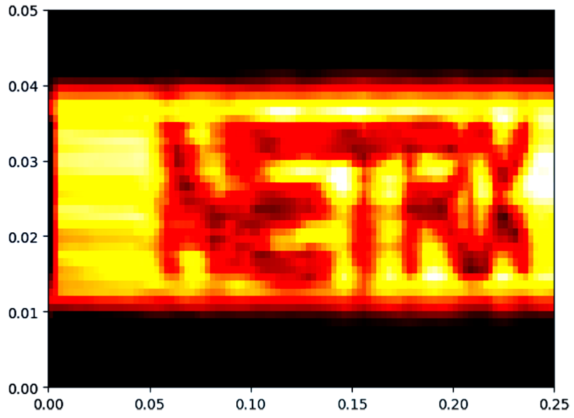

Figure 10. Orthogonal cross-section (YZ-plane) through the reconstructed 3D volume of the "NETRIX" phantom

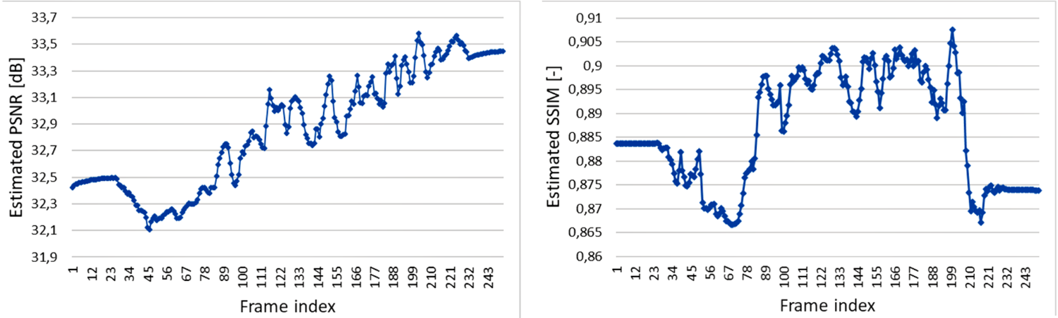

a) b)

Figure 11. Statistical analysis of image quality metrics for each of the 256 frames: (a) distribution of PSNR values [dB], (b) distribution of SSIM values

demand for efficient, portable NDT solutions has never been greater.

The economic case for advanced ultrasonic inspection is compelling. Wind turbine downtime costs operators \$800–\$1.600 per day in lost revenue, while unscheduled maintenance – particularly for blade-related failures – can exceed \$30,000 per repair event [41]. Given that blades typically require inspection and potential repair every 2–5 years, and that blade damage accounts for a disproportionate share of turbine failures, portable systems capable of early defect detection offer substantial cost avoidance opportunities [42].

From an operations-and-maintenance perspective, the value of the proposed approach is driven by turbine availability, the probability of first-time-fix, and the timeliness of degradation detection. The imaging quality already reported (PSNR = 32.0–33.6 dB, SSIM = 0.867–0.908 across 256 frames) indicates stable, metrologically useful volumetric reconstructions under field conditions, which shorten inspections and reduce repeat call-outs. This translates directly into recovered annual energy production (AEP) and lower logistics expenditure.

The revenue recovered from shorter outages can be approximated by $C_{\mathrm{downtime}} = \pi \cdot P_{\mathrm{rated}} \cdot CF \cdot \Delta t$ [43], where π is the wholesale electricity price, P_{rated} the turbine rating, CF the capacity factor, and Δt the reduction in outage hours. Illustratively, for an onshore 4.2 MW turbine with $CF = 0.335$, a 6-hour inspection speed-up at $\pi = 35$\$/MWh recovers about 4.2 × 0.335 × 6 = 8.442 × 6 MWh (≈ 295 \$) per turbine per inspection. For an offshore 12 MW turbine with $CF = 0.50$, the same 6-hour reduction at π = 82 €/MWh yields 12 × 0.5 × 6 = 36 MWh (≈ 2.952 €). In practice, offshore access windows amplify this effect because on-site volumetric sizing accelerates the repair decision.

Earlier mitigation of leading-edge erosion (LEE) produces an additional AEP benefit. Adopting a conservative 3% LEE-related energy loss and advancing intervention by 60 days gives $\Delta E = P_{\mathrm{rated}} \cdot CF \cdot 24 \cdot T \cdot \varepsilon_{LEE}$ [44], which corresponds to roughly 60.8 MWh (≈ 2.128 \$ at 35 \$/MWh) for the 4.2 MW onshore case and 259.2 MWh (≈ 21,254 € at 82 €/MWh) for the 12 MW offshore case. This second channel often outweighs device-level energy savings and reinforces the case for proactive CBM/PHM workflows centered on LEE.

Offshore economics are further strengthened by improved first-time-fix rates that avoid repeat vessel mobilizations: even a single avoided day on a service operation vessel eliminates a large charter cost and, in parallel, prevents roughly one day of lost generation. For a 12 MW turbine with $CF = 0.5$, one day corresponds to 12 × 0.5 × 24 = 144 MWh, i.e., ≈ 11,808 € at 82 €/MWh, in addition to the avoided logistics expenditure. Economically, logistics and recovered AEP commonly co-dominate the return on investment.

Environmental and safety aspects are aligned with these operational gains: compared with radiography, ultrasonic testing avoids ionizing-radiation exposure, relative to penetrant or magnetic particle testing it reduces consumables, and, through energy-efficient embedded processing and digital reporting, the device-level footprint remains secondary to the dominant benefits above.

In a typical maintenance scenario, the proposed system could be used for in-situ blade inspection by mounting the phased-array probe on a small measurement trolley and performing linear scans along selected regions such as the leading edge or bonded joints. During such a scan, preliminary A- and B-scan previews would allow the operator to assess coupling and identify potential indications, while full 3D reconstructions generated afterwards could be used to segment and size volumetric defects and to create a digital inspection report that can be integrated with the wind farm's maintenance management system.

Quantitative evaluation demonstrated PSNR values of 32.0–33.6 dB and SSIM metrics of 0.867–0.908 across 256 sequential frames, indicating image quality comparable to laboratory PAUT systems [45] despite the portable form factor. The low inter-frame variability confirms system stability during scanning operations—essential for automated defect detection pipelines [46]. The delay-and-sum beamforming algorithm, while computationally intensive, has been extensively validated across ultrasonic imaging applications [47] and our implementation on embedded ARM architecture with PyTorch acceleration demonstrates real-time processing feasibility.

The multi-scale Otsu segmentation approach provides adaptive thresholding without manual parameter tuning [34,35], crucial for field operators with varying NDT expertise. While deep learning methods could potentially enhance detection sensitivity [46,48], they require extensive training datasets currently scarce for wind turbine blade defects. Presented classical computer vision pipeline balances robustness with computational efficiency.

Wind turbine blades face multiple degradation mechanisms with significant operational impact. Leading edge erosion (LEE), affecting aerodynamic efficiency and forcing premature blade replacement [49, 50], is particularly critical as rotor diameters increase. Lightning strikes—causing damage ranging from surface scorching to hidden delaminations [51, 52] – require comprehensive volumetric assessment beyond surface inspection capabilities. The 3D point cloud reconstructions enable operators to evaluate full damage extent, including regions beneath intact surface layers.

Offshore wind installations present particular challenges. Downtime per failure for offshore turbines is approximately double that of onshore units [53], with maintenance visits costing $20,000 [54] due to vessel mobilization and weather dependencies. Portable systems enabling comprehensive inspection during limited access windows deliver proportionally higher value in offshore contexts. With 83 GW of offshore capacity installed globally and rapid expansion planned [55], the addressable market for advanced portable NDT is substantial. High first-time detection accuracy reduces repeated inspections, lowering inspector travel, equipment mobilization, and associated environmental footprint. Compared with radiography and penetrant or magnetic particle testing, ultrasonic inspection avoids ionising radiation and minimises consumables, so these operational gains are accompanied by tangible safety and sustainability benefits that align with industry trends toward environmentally responsible inspection practices. Similar concepts of resource efficiency and energy recovery are reported, for example, in the design of low-speed compressed air engines dedicated to energy recovery applications [56].

While the presented results demonstrate high reconstruction fidelity and stable performance of DefectoVision 3D, several limitations should be acknowledged. First, the current implementation relies on a 32–128 element linear array and delay-and-sum beamforming with fixed parameter settings, which may limit sensitivity to very small or low-contrast defects (e.g. defects with characteristic dimensions below 2 mm) and to strongly curved surfaces. The second, the embedded ARM platform imposes constraints on the maximum aperture size, frame rate and reconstruction grid density that can be achieved in real time. Third, measurement quality remains sensitive to coupling conditions, surface roughness and environmental factors such as temperature, which must be controlled during on-site inspections. Fourth, the battery-powered design and integrated thermal management impose constraints on continuous operation time and sustained computational load during high-throughput inspections. Future work will focus on scaling the array aperture, optimising the analogue front-end and embedded software pipeline, and exploring more efficient or hardware-accelerated beamforming schemes to mitigate these constraints.

CONCLUSIONS

The DefectoVision 3D system for ultrasonic nondestructive testing offers not only advanced technical capabilities but also sets new standards for environmental sustainability in industrial inspection. Through its innovative multi-transducer ultrasonic head architecture (32–128 elements), advanced delay-and-sum beamforming algorithms with Hilbert transform–based envelope detection, and an energy-efficient asynchronous Redis-based processing framework, the system enables precise defect localization across one-, two-, and three-dimensional visualization modes. Quantitative validation using established image quality metrics confirms its exceptional performance, with PSNR values ranging from 32.0 to 33.6 dB and SSIM values between 0.867 and 0.908, demonstrating both high reconstruction fidelity and excellent structural preservation.

The energy-efficiency features of DefectoVision 3D set new benchmarks for portable inspection equipment. Dynamic clock scaling, adaptive load management, and intelligent component sleep scheduling reduce power consumption by approximately 40% compared to conventional ultrasonic systems. An automatic shutdown mechanism (triggered after 15 minutes of inactivity) and an optimized battery management system further minimize standby consumption, extending operational time while reducing overall energy requirements. The modular architecture and software-defined functionality also enable future upgrades without hardware replacement, supporting circular economy principles and reducing electronic waste.

High accuracy and reproducibility further minimize the need for repeated inspections, lowering both energy consumption and material usage associated with quality control processes. Performing comprehensive inspections with a single system reduces the environmental footprint compared to maintaining multiple specialized NDT devices. In addition, digital reporting and remote update capabilities decrease the need for physical travel and on-site interventions, contributing to further reductions in carbon emissions.

Future development directions include the integration of machine learning algorithms for automated defect classification, reducing operator dependency and inspection time. Other planned advancements include the use of bio-based composite materials for system components and the implementation of solar-assisted charging for off-grid operation. The system's architecture also supports potential integration with industrial IoT networks for predictive maintenance applications, enabling further optimization of resource use in manufacturing and infrastructure management. In summary, DefectoVision 3D represents not merely a technological advancement in NDT, but a comprehensive sustainable inspection solution that addresses environmental challenges while delivering superior performance. Its combination of technical excellence, energy efficiency, waste reduction, and chemical-free operation establishes a new standard for environmentally responsible industrial inspection technologies aligned with global sustainability goals and circular economy principles.

REFERENCES

1. Bond LJ, Eisenmann D, Meyendorf N, Shepard SM, Burt V, Kelly J, et al. ASM Handbook W Volume 17 Nondestructive Evaluation of Materials Division Editors ASM International Staff n.d.
2. Hellier CJ. Handbook of Nondestructive Evaluation, Second Edition. McGraw-Hill Education; 2013.
3. Visbech J, Göçmen T, Özçakmak ÖS, Meyer Forsting A, Hannesdóttir Á, Réthoré PE. Aerodynamic effects of leading-edge erosion in wind farm flow modeling. Wind Energy Science 2024;9:1811–26. https://doi.org/10.5194/WES-9-1811-2024
4. Contreras López J, Kolios A, Wang L, Chiachio M. A wind turbine blade leading edge rain erosion computational framework. Renew Energy 2023;203:131–41. https://doi.org/10.1016/j.renene.2022.12.050
5. Rose JL. Ultrasonic guided waves in solid media. Ultrasonic Guided Waves in Solid Media 2014;9781107048959:1–512. https://doi.org/10.1017/CBO9781107273610
6. Practice for Radiographic Examination Using Digital Detector Arrays. West Conshohocken, PA: ASTM International; 2018. https://doi.org/10.1520/E2698-18E01
7. Blitz J. Electrical and Magnetic Methods of Non-destructive Testing 1997;3. https://doi.org/10.1007/978-94-011-5818-3
8. Grosse CU, Ohtsu M. Acoustic emission testing: Basics for research-applications in civil engineering. acoustic emission testing: Basics for Research-Applications in Civil Engineering 2008:1–404. https://doi.org/10.1007/978-3-540-69972-9
9. Zhang K, Entezari A. Convolutional forward models for x-ray computed tomography. SIAM J Imaging Sci 2023;16:1953–77. https://doi.org/10.1137/21M1464191
10. Mikulka J. GPU-accelerated reconstruction of T2 maps in magnetic resonance imaging. Measurement Science Review 2015;15:210–8. https://doi.org/10.1515/MSR-2015-0029

11. Soleimani M, Rymarczyk T, Klosowski G. Ultrasound brain tomography: comparison of deep learning and deterministic methods. IEEE Trans Instrum Meas 2023. https://doi.org/10.1109/TIM.2023.3330229
12. Koulountzios P, Rymarczyk T, Soleimani M. Ultrasonic time-of-flight computed tomography for investigation of batch crystallisation processes. Sensors 2021;21:639. https://doi.org/10.3390/S21020639
13. Kulisz M, Kłosowski G, Rymarczyk T, Słoniec J, Gauda K, Cwynar W. Optimizing the neural network loss function in electrical tomography to increase energy efficiency in industrial reactors. Energies (Basel) 2024;17:681. https://doi.org/10.3390/EN17030681
14. Kłosowski G, Rymarczyk T, Niderla K, Kulisz M, Skowron Ł, Soleimani M. Using an LSTM network to monitor industrial reactors using electrical capacitance and impedance tomography – a hybrid approach. Eksploatacja i Niezawodnosc 2023;25. https://doi.org/10.17531/EIN.2023.1.11
15. Korzeniewska E, Gałązka-Czarnecka I, Sekulska-Nalewajko J, Gocławski J, Dróźdż T, Kiełbasa P. Assessment of changes in vitamin content and morphological characteristics in strawberries modified with a pulsed electric field using chromatography and optical coherence tomography. NFS Journal 2025;38. https://doi.org/10.1016/J.NFS.2025.100217
16. Gocławski J, Sekulska-Nalewajko J, Korzeniewska E. Prediction of textile pilling resistance using optical coherence tomography. Sci Rep 2022;12. https://doi.org/10.1038/S41598-022-23230-9
17. Rząsa MR. Selection of optical tomography parameters for gas bubble shape analysis. Chemical and Process Engineering - Inzynieria Chemiczna i Procesowa 2014;35:19–33. https://doi.org/10.2478/CPE-2014-0002
18. Halmshaw R. Industrial radiology : theory and practice 1995:303.
19. Tracy NA., Moore PO. Liquid penetrant testing 1999:493.
20. Maldague X. Chapter 9 - Active thermography. Theory and Practice of Infrared Technology for Nondestructive Testing 2001:177–89.
21. Khan M. Digital detector array for non-destrucitve radiographic imaging of aircraft structures. E-Journal of Nondestructive Testing 2024;29. https://doi.org/10.58286/30024
22. Aminzadeh A, Dimitrova M, Meiabadi MS, Sattarpanah Karganroudi S, Taheri H, Ibrahim H, et al. Non-contact inspection methods for wind turbine blade maintenance: techno–economic review of techniques for integration with industry 4.0. J Nondestr Eval 2023;42:1–20. https://doi.org/10.1007/S10921-023-00967-5/FIGURES/14
23. Krautkrämer J, Krautkrämer H. Ultrasonic testing of materials. ultrasonic testing of materials 1990. https://doi.org/10.1007/978-3-662-10680-8
24. Liu Z, Chen L, Zhu Y, Liu X, He C. Multi-mode high resolution TFM imaging of microdefects based on laser ultrasonic full matrix capture. Opt Laser Technol 2025;181:111913. https://doi.org/10.1016/J.OPTLASTEC.2024.111913
25. Zhao Z, Liu L, Liu W, Teng D, Xiang Y, Xuan FZ. Discretized tensor-based model of total focusing method: A sparse regularization approach for enhanced ultrasonic phased array imaging. NDT & E International 2024;141:102987. https://doi.org/10.1016/J.NDTEINT.2023.102987
26. Duernberger E, MacLeod C, Lines D, Loukas C, Vasilev M. Adaptive optimisation of multi-aperture ultrasonic phased array imaging for increased inspection speeds of wind turbine blade composite panels. NDT & E International 2022;132:102725. https://doi.org/10.1016/J.NDTEINT.2022.102725
27. Przysucha B, Wójcik D, Rymarczyk T, Król K, Kozłowski E, Gąsior M. Analysis of reconstruction energy efficiency in EIT and ECT 3D tomography based on elastic net. Energies 2023;16:1490. https://doi.org/10.3390/EN16031490
28. Rymarczyk T, Niderla K, Kozłowski E, Król K, Wyrwisz JM, Skrzypek-Ahmed S, et al. Logistic regression with wave preprocessing to solve inverse problem in industrial tomography for technological process control. Energies (Basel) 2021;14:8116. https://doi.org/10.3390/EN14238116
29. McMaster RC. Nondestructive testing handbook 1982.
30. Singh RK, Verma HK. Redis-based messaging queue and cache-enabled parallel processing social media analytics framework. Comput J 2022;65:843–57. https://doi.org/10.1093/COMJNL/BXAA114
31. Maharjan R, Chy MSH, Arju MA, Cerny T. Benchmarking message queues. Telecom 2023;4:298–312. https://doi.org/10.3390/TELECOM4020018
32. Corral-García J, González-Sánchez JL, Pérez-Toledano MÁ. Evaluation of strategies for the development of efficient code for raspberry pi devices. Sensors 2018;18:4066. https://doi.org/10.3390/S18114066
33. Goudarzi S, Asif A, Rivaz H. Plane-wave ultrasound beamforming through independent component analysis. Comput Methods Programs Biomed 2020;203. https://doi.org/10.1016/j.cmpb.2021.106036
34. Otsu N. Threshold selection method from Gray-level histograms. IEEE Trans Syst Man Cybern 1979;SMC-9:62–6. https://doi.org/10.1109/TSMC.1979.4310076

35. Liao P-S, Chen T-S, Chung P. A fast algorithm for multilevel thresholding. Journal of Information Science and Engineering 2001. https://doi.org/10.6688/JISE.2001.17.5.1
36. Wang Z, Bovik AC, Sheikh HR, Simoncelli EP. Image quality assessment: From error visibility to structural similarity. IEEE Transactions on Image Processing 2004;13:600–12. https://doi.org/10.1109/TIP.2003.819861
37. Horé A, Ziou D. Image quality metrics: PSNR vs. SSIM. Proceedings - International Conference on Pattern Recognition 2010:2366–9. https://doi.org/10.1109/ICPR.2010.579
38. Wind Turbine Blade Inspection Services Market Share Report 2025 n.d. https://www.thebusinessresearchcompany.com/report/wind-turbine-blade-inspection-services-global-market-report (accessed November 4, 2025).
39. Global Statistics n.d. https://wwindea.org/Global-Statistics (accessed November 4, 2025).
40. How Many Wind Turbines Are There In The World? - AEANET n.d. https://www.aeanet.org/how-many-wind-turbines-are-there-in-the-world/?utm_source=chatgpt.com (accessed November 4, 2025).
41. Mishnaevsky L, Thomsen K. Costs of repair of wind turbine blades: Influence of technology aspects. Wind Energy 2020;23:2247–55. https://doi.org/10.1002/WE.2552
42. Budisetyawan D, Adiputra R, Prabowo AR, Erwandi E. The tendency of failure probability on offshore wind turbine components: A review. Lecture Notes in Mechanical Engineering 2024:609–13. https://doi.org/10.1007/978-981-97-0106-3_96
43. Wind Energy and Power Calculations | EM SC 470: Applied Sustainability in Contemporary Culture n.d. https://www.e-education.psu.edu/emsc297/node/649?utm_source=chatgpt.com (accessed November 6, 2025).
44. Visbech J, Göçmen T, Özçakmak ÖS, Meyer Forsting A, Hannesdóttir Á, Réthoré PE. Aerodynamic effects of leading-edge erosion in wind farm flow modeling. Wind Energy Science 2024;9:1811–26. https://doi.org/10.5194/WES-9-1811-2024
45. Zhu J, Wang G, Luo K, Zhang X. Ultrasonic nondestructive testing image enhancement model based on super-resolution imaging. Applied Sciences 2025;15:8339. https://doi.org/10.3390/APP15158339
46. Cantero-Chinchilla S, Wilcox PD, Croxford AJ. Deep learning in automated ultrasonic NDE – Developments, axioms and opportunities. NDT & E International 2022;131:102703. https://doi.org/10.1016/J.NDTEINT.2022.102703
47. Matrone G, Savoia AS, Caliano G, Magenes G. The delay multiply and sum beamforming algorithm in ultrasound B-mode medical imaging. IEEE Trans Med Imaging 2015;34:940–9. https://doi.org/10.1109/TMI.2014.2371235
48. Sun H, Ramuhalli P, Meyer R. An Assessment of Machine Learning Applied to Ultrasonic Nondestructive Evaluation 2023.
49. Mishnaevsky L, Hasager CB, Bak C, Tilg AM, Bech JI, Doagou Rad S, et al. Leading edge erosion of wind turbine blades: Understanding, prevention and protection. Renew Energy 2021;169:953–69. https://doi.org/10.1016/J.RENENE.2021.01.044
50. Eisenberg D, Laustsen S, Stege J. Wind turbine blade coating leading edge rain erosion model: Development and validation. Wind Energy 2018;21:942–51. https://doi.org/10.1002/WE.2200
51. Mishnaevsky L. Root causes and mechanisms of failure of wind turbine blades: overview. Materials 2022;15:2959. https://doi.org/10.3390/MA15092959
52. Katsaprakakis D Al, Papadakis N, Ntintakis I. A comprehensive analysis of wind turbine blade damage. Energies (Basel) 2021;14:5974. https://doi.org/10.3390/EN14185974
53. Lorentzen S, Osmundsen P, Lu L. Immature offshore wind technology: UK life cycle capacity factor analysis. Wind Energy 2024;27:1095–110. https://doi.org/10.1002/WE.2939
54. Zappalá D, Tavner PJ. Wind turbine reliability – maintenance strategies. Comprehensive Renewable Energy, Second Edition: 2022;1–9:353–70. https://doi.org/10.1016/B978-0-12-819727-1.00154-0
55. GWEC's Global Offshore Wind Report n.d. https://www.gwec.net/reports/globaloffshorewindreport (accessed November 4, 2025).
56. Rząsa M, Łukasiewicz E, Wójtowicz D, Rząsa M, Łukasiewicz E, Wójtowicz D. Test of a new low-speed compressed air engine for energy recovery. Energies (Basel) 2021;14. https://doi.org/10.3390/EN14041179